Secondary aerosol formation under a special dust transport event: impacts from unusually enhanced ozone and dust backflows over the ocean

Da Lu[1], Hao Li[1], Guochen Wang[1], Mengke Tian[1], Xiaofei Qin[1], Na Zhao[1], Juntao Huo[2], Fan Yang[3], Yanfen Lin[2], Jia Chen[2], Qingyan Fu[2], Yusen Duan[2], Xinyi Dong[4], Congrui Deng[1], Sabur F. Abdullaev[5], Kan Huang[1,6*]

[1]Center for Atmospheric Chemistry Study, Shanghai Key Laboratory of Atmospheric Particle Pollution and Prevention (LAP[3]), National Observations and Research Station for Wetland Ecosystems of the Yangtze Estuary, Department of Environmental Science and Engineering, Fudan University, Shanghai, 200433, China

[2]State Ecologic Environmental Scientific Observation and Research Station for Dianshan Lake, Shanghai Environmental Monitoring Center, Shanghai, 200030, China

[3]Pudong New District Environmental Monitoring Station, Shanghai 200122, China

[4]School of Atmospheric Sciences, Nanjing University, Nanjing 210023, China

[5]Physical Technical Institute of the Academy of Sciences of Tajikistan, Dushanbe, Tajikistan

[6]Institute of Eco-Chongming (IEC), Shanghai, 202162, China

Corresponding author: huangkan@fudan.edu.cn

Abstract

In the autumn of 2019, a five-day long-lasting dust event was observed using a synergy of field measurement techniques in Shanghai. This particular dust event stood

out from others due to its unique characteristics, including low wind speed, high relative humidity, elevated levels of gaseous precursors, and contrasting wind patterns at different altitudes. During this event, three distinct dust stages were identified. The first stage was a typical dust invasion characterized by ~~with~~ high concentrations of particulate matters but relatively short duration. In contrast, the second stage exhibited an unusual enhancement of ozone, attributed to compound causes of weak synoptic system, transport from the ocean, and subsidence of high-altitude ozone down drafted by dust. Consequently, gas phase oxidation served as the major formation pathway of sulfate and nitrate. In the third stage of dust, a noteworthy phenomenon known as dust backflow occurred. The dust plume originated from the Shandong Peninsula and slowly drifted over the Yellow Sea and the East China Sea before eventually returning to Shanghai. Evidence of this backflow was found through the enrichment of marine vessel emissions (V and Ni) and increased solubility of calcium. Under the influence of humid oceanic breezes, the formation of nitrate was dominated by aqueous processing. Additionally, part of nitrate and sulfate were directly transported via sea salts, evidenced by their co-variation with Na^+ and confirmed through thermodynamic modeling. The uptake of NH_3 on particles, influenced by the contributions of alkali metal ions and aerosol pH, regulated the formation potential of secondary aerosol. By developing an upstream-receptor relationship method, the amounts of transported and secondarily formed aerosol species were separated. This study highlights that the transport pathway of dust, coupled with environmental conditions, can significantly modify the aerosol properties, especially at the complex land-sea interface.

1. Introduction

49   Dust serves as a significant natural source of aerosols, constituting approximately

50 half of the tropospheric aerosols (Zheng et al., 2016). Dust aerosols play crucial roles

51 in environmental and climatic changes by affecting the radiation balance (Feng et al.,

52 2020; Nagashima et al., 2016; Goodman et al., 2019). The optical properties of dust

53 aerosols are influenced by various parameters of iron oxides, including refractive

54 indices, size distributions, and mineralogical compositions. Consequently, these factors

55 introduce potential uncertainties regarding the role of dust in climate forcing (Zhang et

56 al., 2015; Jeong, 2008). Furthermore, dust aerosols have important impacts on

57 tropospheric chemistry by participating in heterogeneous and photolysis reactions in

58 the atmosphere (Wang et al., 2014; Liu et al., 2018). During transport, dust can mix

59 with gaseous pollutants, toxic metals, and soot, thereby affecting air quality

60 immediately and potentially posing public health hazards (Liu et al., 2021; Wang et al.,

61 2021). Moreover, Barkley et al. (2021) found that iron-containing aerosols transported

62 from Africa to the equatorial North Atlantic Ocean provided plentiful nutrients to algae

63 in the ocean and accumulated inside algae.

64   The irregular shapes of dust particles provide an efficient medium for

65 heterogeneous reactions with NO_2, O_3, SO_2, and NH_3, thereby altering the particle size

66 spectrum, hygroscopicity, and radiative properties (Hsu et al., 2014; Tian et al., 2021;

67 Jiang et al., 2018). Jiang et al. (2018) observed a significant increase in nitrate and

68 sulfate concentrations during a dust period in March 2010 in Shanghai. This elevation

69 was attributed to the presence of moderate to high levels of relative humidity and

70 gaseous precursors, implying that dust can efficiently promote the formation of sulfate

71 and nitrate. Previous studies have revealed that HNO_3 formed through the reactions of

72 NO_2 with hydroxyl radical or N_2O_5 hydrolysis preferentially reacts with mineral dust

73 particles and produce nitrate, which serves as the primary source of nitrate during dust

74 episodes (Tang et al., 2016; Wu et al., 2020). Improvements in the simulation of sulfate

75 were achieved by employing various parameterization schemes for the heterogeneous

76 uptake of SO_2 on natural dust surfaces in the presence of NH_3 and NO_2 under different

77 relative humidity conditions(Zhang et al., 2019). Wang et al. (2018) simulated that

78 heterogeneous reactions on dust accounted for the majority of nitrate over the Yellow

79 Sea and the East China Sea during the dust long-range transport. Tang et al. (2017)

80 conducted a comprehensive review on the effect of dust heterogeneous reactions on the

81 tropospheric oxidation capacity. They proposed that high RH (> 80%) and a wider range

82 of temperature should be considered in the laboratory studies of heterogeneous

83 reactions of mineral dust. Additionally, more comprehensive kinetic models should be

84 developed to understand the complex multiphase reactions.

85   Controversies have arisen regarding the mixing of dust and anthropogenic aerosols.

86 Zhang et al. (2005) found that anthropogenic aerosols separated with dust during a dust

87 event in Qingdao, China. Coincidentally, a time-lag between dust and anthropogenic

88 aerosols was observed in Japan and South Korea downstream of the dust transport.

89 Single particle analysis revealed that sulfate in fine particles appeared 12 hours before

90 the dust arrival in Japan. Wang et al. (2013) also observed a lag of 10 - 12 hours between

91 dust and anthropogenic aerosols on a dust day in Shanghai (Wang et al., 2013).

92 Furthermore, Huang et al. (2019) documented vertical differences in long-transported

93 aerosols during a pollution event in Taiwan. Dust from the Gobi Desert in Inner

94 Mongolia and China existed at the altitudes of 0.8km and 1.90km, respectively, while

95 biomass burning aerosols from South Asia were present at higher altitudes of 3.5km.

96 Coastal regions often experience a mixture of inland anthropogenic emissions and

97   releases from the ocean, making regional pollution complex in these areas   (Wang et

98   al.; Hilario et al., 2020; Patel and Rastogi, 2020; Perez et al., 2016; Wang et al., 2017).

99   The eastern coast of China, bordering the East China Sea and the Yellow Sea, is

100 particularly influenced by the Asian monsoon and high emissions from inland industries,

101 resulting in highly intricate meteorological and pollution conditions (Hilario et al.,

102 2020). Furthermore, the marine boundary layer in this region exhibits significant

103 seasonal and diurnal variations in , relative humidity and temperature further impacting

104 photochemical processes and heterogeneous reactions on aerosol surfaces (Zhao et al.,

105 2021). Sea and land breezes play a crucial role in this coastal area. During the night,

106 land breezes carry pollutants from the land to the sea. Subsequently, during the day,

107 these land breezes transform into sea breezes, bringing the pollutants back over the sea.

108 This phenomenon leads to an increase in air pollutants over the land (Zhao et al., 2021).

109 For instance, Wang et al. (2022b) found that during the ozone pollution in Shanghai in

110 2018, the presence of O_3 at high altitudes at night was transported vertically downward

111 during the daytime and high O_3 over the ocean was transported horizontally to the land,

112 jointly contributing to regional O_3 pollution in Shanghai. Also, one dust episode in 2014

113 was observed over Shanghai via detouring from northern China due to the blocked north

114 Pacific subtropical high-pressure system (Wang et al., 2018).

115   Previous studies have shown that about 70% of Asian dust traverses the eastern

116 coast of China before moving towards the Korean Peninsula, the Sea of Japan, and

117 eventually reaching the Pacific Ocean. The eastern coast of China serves as a crucial

118 route for Asian dust transport to the Pacific Ocean (Arimoto et al., 1997; Huang et al.,

119 2010a). Most previous research has focused on typical dust events characterized by

120 strong intensities, high wind speed, low humidity, and low oxidants (Li et al., 2017; Ma

121 et al., 2019; Xu et al., 2017; Xie et al., 2005). In contrast, this study aims to depict an

122 atypical dust event that was observed in Shanghai, a coastal mega-city in Eastern China.

123 The unusualness of the meteorological conditions, transport pathways, and air

124 pollutants during the particular dust event was explicitly described. The study involves

125 categorizing the dust event into three stages and comparing the aerosol chemical

126 compositions between these stages. By focusing on the second and third stages, the

127 different formation mechanisms of nitrate and sulfate were investigated. The amounts

128 of major aerosol species from transport and secondary formation were estimated based

129 on a simplified method of relating the upstream and receptor simultaneous

130 measurements.

131

132 **2. Methodology**

133 **2.1. Observational sites**

134   At Shanghai Pudong Environmental Monitoring Station (31°13′ N, 121°32′E),

135 comprehensive measurements of various atmospheric parameters were conducted.

136 All the instruments were installed on the top floor of a building, about 25m above

137 the ground level. As shown in Figure S1, the sampling site is situated at the eastern

138 tip of Shanghai, close to the coastal line. During November, the mean temperature

139 and relative humidity in Shanghai were recorded as 17.3℃ and 72% respectively.

140 In autumn and winter, air pollutants originating from upstream urban regions often

141 undergo transport to Shanghai via high-pressure systems. Additionally, air

142 pollutants in Shanghai tended to linger at the sea/land boundary regions due to the

143 sea-land breeze (Shen et al., 2019).

144   In addition to the measurements taken in Shanghai, data from environmental

145   monitoring stations in Qingdao and Lianyungang are also incorporated into this

146   study.

147

148   **2.2. Instrumentation**

149   A set of online instruments was set up at the Pudong observational site. Inorganic ions

150   (NO_3^-, SO_4^{2-}, Cl^-, Na^+, NH_4^+, K^+, Mg^{2+}, Ca^{2+}) in $PM_{2.5}$ and soluble gases (NH_3, HNO_3,

151   HCl, HONO) were measured by an online ion chromatography (IC, MARGA-1S,

152   Metrohm). It operated at a flow rate of 16.7 L/min with a time resolution of one hour.

153   Briefly, air was drawn into a $PM_{2.5}$ cyclone inlet and passed through a wet rotating

154   denuder (gases) and a steam jet aerosol collector (aerosols). Subsequently, the aqueous

155   samples were analyzed with ion chromatography. More details can be found in (Xu et

156   al., 2020). Hourly trace metals (Si, Ca, Cu, Fe, K, Co, Mn, Cr, Zn, Pb, As, Cd, V, Ni) in

157    $PM_{2.5}$ were measured by using the Xact 625 multi-metals monitor (Cooper

158   Environmental, Beaverton, OR, USA). Particles were collected onto a Teflon filter tape

159   at a flow rate of 16.7 L/min, and then transported into the spectrometer where the

160   particles were analyzed with an X-ray fluorescence. Organic carbon and elemental

161   carbon were measured by an in situ Semi-Continuous Organic Carbon and Elemental

162   Carbon aerosol analyzer (RT-4, Sunset Laboratory, Beaverton, Oregon, USA). Samples

163   were collected for 40 min and then analyzed in the following 20 min. The concentration

164   of mineral aerosols is calculated by summing the major mineral elements with oxygen

165   for their normal oxides, i.e., [Minerals]= (2.2*Al+2.49*Si+1.63*Ca+2.42*Fe+1.94*Ti)

166   (Malm et al., 1994). The concentration of OM (organic matters) is estimated by

167   multiplying OC with a factor of 2.

168   The concentrations of particles and gaseous pollutants were measured by a set of

169 Thermo Fisher Scientific instruments, including PM$_{2.5}$ (Thermo 5030i), PM$_{10}$ (Thermo

170 5030i), SO$_2$ (Thermo Fisher 43i), NO$_x$ (Thermo Fisher 42i), O$_3$ (Thermo Fisher 49i),

171 and CO (Thermo Fisher 48i-TLE). These parameters were measured at the temporal

172 resolution of 5min. Meteorological parameters (ambient temperature, relative humidity,

173 wind speed, and wind direction) were obtained by a Vaisala Weather transmitter

174 (WXT520) at the temporal resolution of 1min. Other supplementary parameters such

175 as tThe height of planetary boundary layer (PBL) was retrieved from a ceilometer

176 (CL31, Vaisala) at the temporal resolution of 30 min., vVertical profiles of ozone and

177 aerosol optical properties extinction were obtained by an aerosol lidar (AGJ, AIOFM)

178 at the temporal resolution of 30 min and vertical resolution of 7.5 m, respectively.a

179 ceilometer (CL31, Vaisala), Vertical profiles of ozone were obtained by an ozone lidar

180 (LIDAR-G-2000, WUXIZHONGKE) at the temporal resolution of 15 min and vertical

181 resolution of 7.5 m, respectively., and aerosol lidar (AGJ, AIOFM), respectively. All

182 instruments are routinely maintained and calibrated to ensure the quality of data.

183

184 **2.3. Thermodynamic simulation of aerosol pH and aerosol liquid water content**

185   The ISORROPIA II model is subject to the principle of minimizing the Gibbs energy

186 of the multi-phase aerosol system, leading to a computationally intensive optimization

187 problem (Song et al., 2018). The model can predict the physical state and compositions

188 of atmospheric inorganic species (NH$_4^+$, Na$^+$, K$^+$, Mg^{2+}, Ca^{2+}, SO$_4^{2-}$, NO$_3^-$ and Cl$^-$)

189 with their gas- and particle-phase concentrations and meteorological parameters

190 (relative humidity and temperature) as model inputs. The model includes two modes,

191 i.e., reverse and forward mode. The reverse mode calculates the equilibrium

192 partitioning based on aerosol-phase concentrations only, while the latter uses both

193 aerosol-phase and gas-phase concentrations as inputs. Moreover, particles can be

194 assumed as "metastable" with liquid-phase but no solid participating while "stable"

195 with the liquid and solid phases or both. The ISORROPIA running in the forward mode

196 at the metastable state was applied in this study. Aerosol pH was calculated based on

197 the equilibrium particle hydronium ion concentration and aerosol liquid water content

198 (ALWC) obtained from model results. ~~ISORROPIA II calculates the aerosol pH, ALWC~~

199 ~~(aerosol liquid water content) and compositions of ammonia sulfate nitrate chloride~~

200 ~~sodium calcium potassium magnesium in the thermodynamic equilibrium with gas~~

201 ~~phase precursors.~~ The performances and advantages of ISORROPIA over the usage of

202 other thermodynamic equilibrium codes has been assessed in numerous studies (Nenes

203 et al., 1998; West et al., 1999; Ansari and Pandis, 1999; Yu et al., 2005). ~~The~~

204 ~~ISORROPIA running in the forward mode at the metastable state was applied in this~~

205 ~~study.~~

206

207 **2.4. Hybrid Single-Particle Lagrangian Integrated Trajectory Model**

208   The HYSPLIT (Hybrid Single-Particle Lagrangian Integrated Trajectory) was

209 used to compute the backward trajectories of the air parcels during the dust events. It is

210 a widely used model that computes dispersion following the particle or puff. The

211 advection of a particle or puff is computed from the average of the three-dimensional

212 velocity vectors for the initial position and the first-guess position (Draxler

213 and Hess, 1998). Turbulent velocity components are expressed as a function of the

214 velocity variance, a statistical quantity derived from the meteorological data, and the

215 Lagrangian time scale. The calculation of air mass trajectories can be used to depict the

216 airflow patterns for interpreting the transport of air pollutants over various spatial and

217 temporal ranges (Stein et al., 2015). In this study, the HYSPLIT model was driven by

218 meteorological data outputs from the Global Data Assimilation System (GDAS) (Su et

219 al., 2015), which is available at ftp://arlftp.arlhq.noaa.gov/pub/archives/gdas1. Air mass

220 trajectories were launched at different heights from the ground and a total duration of

221 48 hours simulation was conducted.

222

223 **2.5. Calculation of uptake coefficient of NH₃ (γ NH3) on particles**

224 NH$_3$, being the most abundant alkaline species in the atmosphere, plays a crucial

225 role in acid neutralization and secondary aerosol formation. To assess the gas-particle

226 partitioning of NH$_3$, the uptake coefficient of NH$_3$ (γ_{NH3}) on particles is calculated as

227 below. Initially, the quasi-first-order reaction rate constant for heterogeneous

228 conversion from NH$_3$ to NH$_4^+$ (k_{het}, s^{-1}) is calculated is calculated by Eq. (1)according

229 to (Liu et al., 2022).

230
$$k_{het} = \frac{2(C_{NH_4^+,t_2} - C_{NH_4^+,t_1})}{(C_{NH_3,t_2} + C_{NH_3,t_1})(t_2 - t_1)} \quad (1)$$

231 k_{het} is only valid when c_{NH4+} increases, while c_{NH3} decreases assuming a constant

232 emission rate from t$_1$ to t$_2$ (1 h in this study). Then, the uptake coefficient of NH$_3$ (γ_{NH3})

233 on particles can be calculated as below (Liu et al., 2022; Wang and Lu, 2016).

234
$$\gamma_{NH_3} = \frac{4k_{het}}{S\omega} = \frac{4k_{het}}{S\sqrt{\frac{8RT}{\pi M}}} \quad (2)$$

235 where S is the surface area of particles (m^2 m^{-3}) measured using SMPS and APS. ω is

236 the velocity of NH$_3$ molecules. T is the ambient temperature (K). R is the ideal gas

237 constant, and M is the molecular weight of NH$_3$ (kg mol^{-1}).

238

239 **3. Results and Discussion**

3.1. Characteristics of an unusual dust event

Figure 1 shows the time series of PM_{10}, $PM_{2.5}$, meteorological parameters, as well as the vertical profiles of aerosol extinction coefficient and depolarization ratio observed at the Shanghai sampling site from October 25 to November 6, 2019. From October 25 to 28, the mean wind speed was 0.9±0.72m/s with a peak value of 3.1m/s, remaining relatively low, and predominantly blowing from the northwest~~remained relatively low of 0.9±0.72m/s with a peak value of 3.1m/s, and predominantly blowing from the northwest~~. The mean concentrations of $PM_{2.5}$ and PM_{10} ~~was~~ were 34.7 and 44.2 μg/m^3, respectively. Starting at 4:00 LST on October 29, the concentration of PM_{10} increased sharply and lasted till November 2 (Figure 1d). The aerosol lidar observation indicated that both the aerosol extinction coefficient and depolarization ratio extended from the ground to around 2km during the same period. In general, if the particle depolarization ratio exceeds 10%, the aerosol is identified as mineral dust (Shimizu et al., 2004) due to the nonsphericity (irregular shapes) and relatively large size of particles (Mcneil and Carswell, 1975). Notably, the enhanced depolarization ratio (>0.1) suggested the occurrence of a prolonged dust event in Shanghai. By using the $PM_{2.5}/PM_{10}$ mass ratio of 0.4 as a threshold (Fan et al., 2021), the period from October 29 to November 2 was defined as the dust period in this study. The remaining days, including October 25 to October 28 and November 3 to November 6, were defined as the non-dust period. Throughout the entire dust period, the mean concentrations of $PM_{2.5}$ and PM_{10} reached 53.3 ± 20.5μg/m^3 and 172.4 ± 70.2μg/m^3, respectively, yielding a low $PM_{2.5}/PM_{10}$ ratio of 0.34 ± 0.15. As a comparison, $PM_{2.5}$ and PM_{10} during the non-dust period was 38.9μg/m^3 and 49.8μg/m^3, respectively, exhibiting a relatively high $PM_{2.5}/PM_{10}$ ratio of 0.62 ± 0.20.

264

265
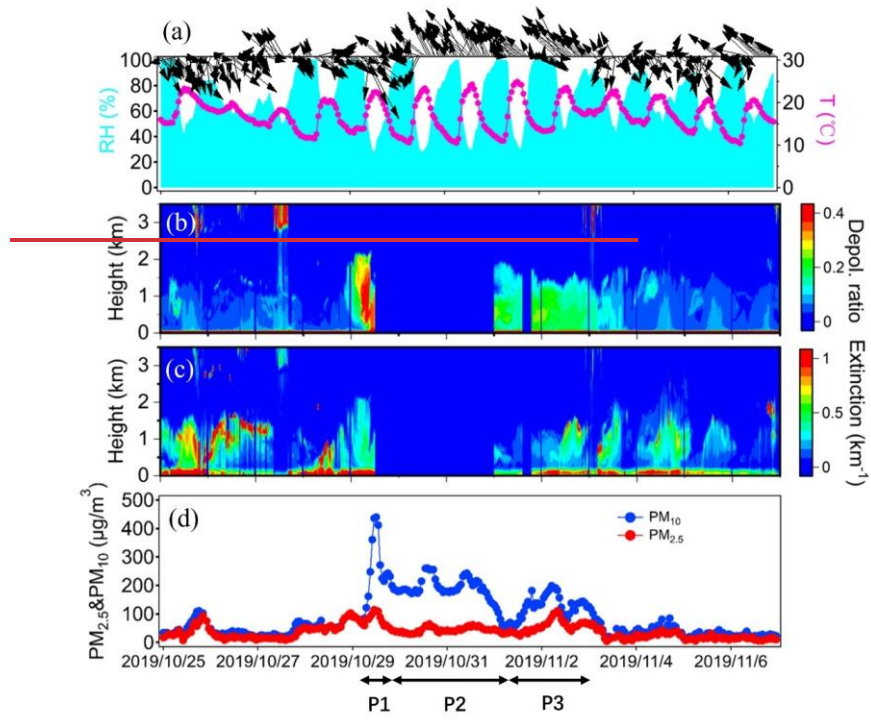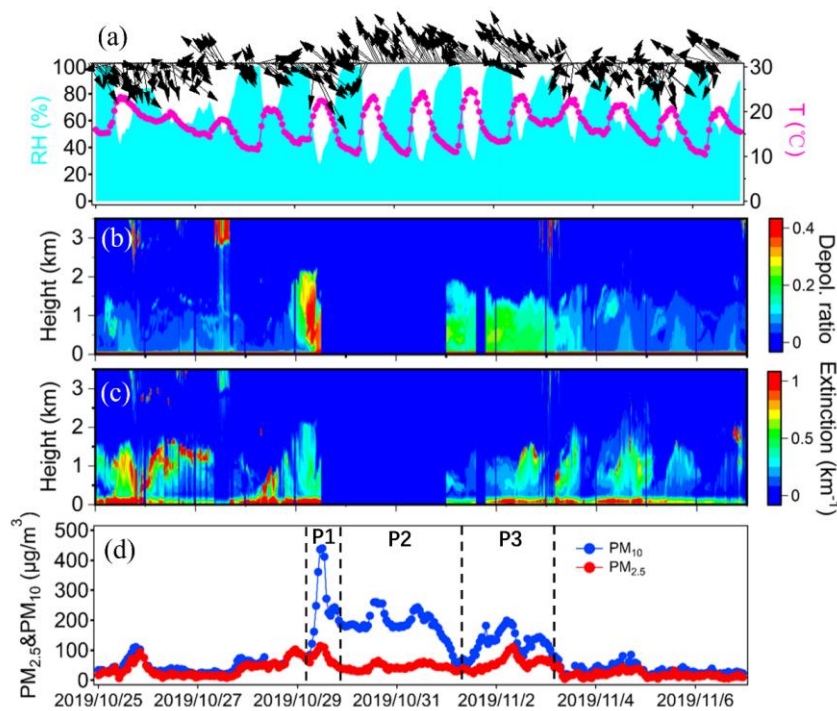
Figure 1. Time series of (a) relative humidity, temperature, wind vectors, (b) aerosol
depolarization ratio, (c) aerosol extinction coefficient, (d) mass concentrations of $PM_{2.5}$
and PM_{10} during the study period. Three dust stages, i.e., P1, P2, and P3 are also marked.
The missing aerosol lidar data were due to instrument malfunction.

The occurrences of dust are typically accompanied by low relative humidity and
strong winds due to the passage of cold fronts (~~Huang et al., 2010b;~~ Huang et al., 2010a;
Wang et al., 2013; Wang et al., 2018). However, in this study, relative humidity was
exceptionally high with the mean value of 71±26%. It showed strong diurnal variation,
reaching its minimum in the daytime and even close to 100% in the nighttime (Figure
1a). Additionally, wind speed was low of 0.54±0.59m/s with a maximum of 2.6m/s.
This stagnant synoptic condition led to elevated concentrations of main gaseous

278 pollutants such as O_3, SO_2, and NO_2, with mean values of $86.0\pm47.8\mu g/m^3$,

279 $11.8\pm3.4\mu g/m^3$, and $63.3\pm27.9\mu g/m^3$, respectively, even higher than those during the

280 non-dust period.

281   We further divided the dust event into three stages based on the temporal

282 characteristics of PM_{10} and the transport patterns of air masses. As shown in Figure 1d,

283 PM_{10} quickly climbed from 4:00 on October 29 and reached a maximum of $436\mu g/m^3$

284 after 8 hours. The air masses primarily originated from the semi-arid regions of

285 northwest China (Figure 2d), which was consistent with both the near surface wind

286 observation (Figure 1a) and wind lidar observation (Figure 2a). The wind profiles

287 showed prevailing northwest winds from the surface up to around 2km before noon on

288 October 29, indicating the presence of a strong synoptic system. Afterwards, PM_{10}

289 quickly decreased to 199 $\mu g/m^3$ at 20:00, October 29 within 8 hours. This was primarily

290 attributed to the shift of wind directions. As shown in Figure 2a, while winds above

291 700m continued to blow from the northwest, near- surface winds had shifted from the

292 southeast. Due to Shanghai's coastal location adjacent to the East China Sea, the

293 relatively clean southeasterlies diluted the local air pollutants, thereby explaining the

294 quick decline in PM10 concentrations. This initial dust episode occurring from 4:00 -

295 13:00 on October 29 was defined as Stage P1.

296   Despite the persistent southeasterly winds, the dust event did not come to a

297 complete halt. Even under these prevailing winds, hourly PM_{10} concentrations

298 remained above 150 $\mu g/m^3$ until November 1, gradually decreasing to 65 $\mu g/m^3$ at 03:00,

299 November 1 (Figure 1d). Compared to P1, wind speed during this stage was as low as

300 $0.4 \pm 0.5m/s$, while RH was moderately high of $70 \pm 26\%$. Although the daytime RH

301 stayed low between 30% and 50%, it frequently soared above 90% at nighttime. Figure

2e shows that although the air masses originated from the Gobi Desert, they also traversed considerable coastal regions. The wind profiles further indicated that while northwest winds prevailed at altitudes higher than 500m, east and northeast winds were dominant below 500m (Figure 2b). Consequently, the relatively high RH during this period can be attributed to the mixing of dust plumes with coastal sea breezes. This dust episode from 14:00, October 29 to 3:00 on November 1 was designated as Stage P2.

Following P2, PM_{10} and $PM_{2.5}$ rose again and peaked at 5:00 and 9:00 on November 2 with the hourly concentration of 199 and $117\mu g/m^3$, respectively. Different from P1 and P2, the air masses during this stage originated from the Shandong Peninsula and the northern region of Jiangsu province, and then migrated over the Yellow Sea and the East China Sea (Figure 2f). Typically, dust plumes tend to travel eastward, impacting the western Pacific region and even distant oceanic regions (Wang et al., 2018; Nagashima et al., 2016). However, in this case, the air masses evidently deviated and pushed the dust back towards the mainland. The wind profiles on November 2 revealed that winds within the detected altitude range predominantly originated from the eastern and southeastern oceanic regions (Figure 2c). This probably indicated the mixing between dust plumes and humid oceanic air masses was quite sufficient, which was also reflected by the highest average RH of $76 \pm 24\%$ among the three stages of the dust event. Moreover, the concentrations of O_3 and NO_2 at this stage were higher than those of P1 and P2, potentially promoting the formation of secondary aerosol components and will be discussed later. This rarely observed dust backflow transport episode from 4:00 on November 1 to 23:00 on November 2 was designated as Stage P3.
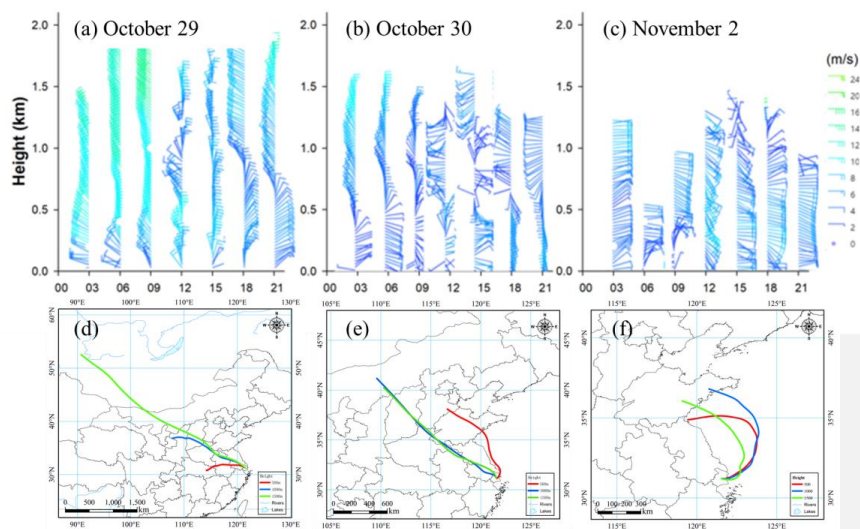
Figure 2. Wind profiles observed by a wind profiler radar on (a) October 29, (b) October 30, and (c) November 2. 48-hour backward trajectories simulated at the sampling site starting from (d) 4:00 AM, October 29, (e) 9:00 AM, October 30, and (f) 13:00 PM, November 2. The red, blue, and green trajectories represented starting altitudes of 100, 500, and 1500m, respectively.

3.2. Comparisons of aerosol chemical compositions among the three dust stages

Figure 3a shows the time-series of hourly aerosol chemical components, including SNA (NO_3^-, SO_4^{2-}, and NH_4^+), OM, EC, and mineral aerosols in $PM_{2.5}$. During P1, the mean concentration of SNA was 49.9 ± 31.6 μg/m^3. The mineral aerosols reached 16.4 ± 14.6 μg/m^3, accounting for 19% in $PM_{2.5}$. The contribution of

337 OM to PM$_{2.5}$ was almost identical to that of mineral aerosols (Figure 3b).

338
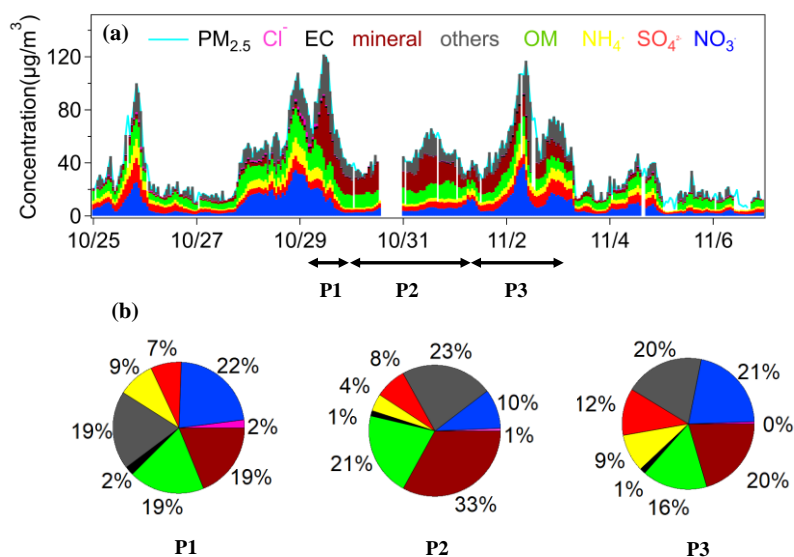
339
340 Figure 3. (a) Times-series of major chemical components in PM$_{2.5}$ during the study
341 period. (b) The mean proportion of major chemical components in PM$_{2.5}$ during the
342 three dust stages.

343

344   During P2, mineral aerosols increased to 23.4±54.1μg/m^3 and accounted for 33%

345 in PM$_{2.5}$, representing the highest among all three stages (Figure 3b). Due to the

346 continuous dilution effect of dust on local anthropogenic pollutants, the concentrations

347 and proportions of SNA in PM$_{2.5}$ were the lowest during this stage. For instance, NO$_3^-$

348 only accounted for 10% in PM$_{2.5}$, indicating a suppression of nitrate formation to some

349 extent. The levels of OM didn't exhibit obvious changes and averaged 10.1±2.1μg/m^3,

350 accounting for 21% in PM$_{2.5}$.

351   During P3, mineral aerosols averaged 11.9±2.7μg/m^3, ranking the lowest among

352 all three stages. The proportion of mineral aerosols in PM$_{2.5}$ decreased to 20%,

353 suggesting the dust backflow from the ocean was less enriched in mineral components.

354 Compared to P2, SNA showed significant increases and much stronger diurnal

355 variations during P3. SO_4^{2-}, NO_3^-, and NH_4^+ averaged 6.7 ± 2.4, 12.4 ± 8.9, and $5.4 \pm$

356 $2.7 \mu g/m^3$, respectively. As shown in Figure 3b, the contribution of nitrate to $PM_{2.5}$

357 increased to 21%, while that of sulfate rose to 12%, the highest among all three stages.

358 The concentration of OM ($9.3 \pm 3.2 \mu g/m^3$) and its proportion (16%) during P3 were

359 lower than the other two stages, likely due to the unconventional dust backflow

360 transport pathway.

361

362 **3.3. Unconventional features of the dust episodes**

363 **3.3.1. Unusually enhanced O₃ during dust**

364   Figure 4 shows the hourly near surface ozone concentrations and vertical profiles

365 of ozone during the study period. Interestingly, a few high O_3 peaks occurred during

366 the dust event (Figure 4a). O_3 averaged $92.8 \pm 52.8 \mu g/m^3$ during the dust, about 50%

367 higher than the non-dust days. Among the three dust stages, O_3 substantially increased

368 from $35.9 \pm 36.4 \mu g/m^3$ during P1 to $80.7 \pm 41.2 \mu g/m^3$ during P2, and further rose to

369 $104.0 \pm 48.7 \mu g/m^3$ during P3. The low O_3 during P1 can be attributed to the cleansing

370 effect of the strong dust associated with the cold front, which was consistent with

371 previous studies that reported reduced oxidant concentrations during intense dust

372 events (Benas et al., 2013). Regarding the relatively high O_3 during P2 and P3, several

373 causes may contribute to this phenomenon. Firstly, the mean wind speed was low of

374 0.4 and 0.6 m/s during P2 and P3, respectively. ~~Consequently, this weak synoptic~~

375 ~~system exerted a weak dilution effect on the local air pollutants.~~ OneA numerical

376 study conducted during thea similar period suggested that the low wind speed caused

377 ~~the~~ reduction of boundary layer height and the warming of the lower atmosphere, thus

378 accelerat~~ing~~ed the ozone formation by ~1 ppbv/h (Wang et al., 2020). Consequently,

379 this weak synoptic system was favorable for the accumulation of ozone~~exerted a weak~~

380 ~~dilution effect on the local air pollutants.~~ Secondly, since the dust plume travelled

381 mostly over the coastal and oceanic areas, a portion of O_3 could be transported from

382 the high ozone oceanic areas (Wang et al., 2022b). Thirdly, the ozone lidar also

383 detected high O_3 stripes during P2 and P3. As shown in ~~Figure 5b~~Figure 4b, the high

384 O_3 profiles extended from the surface to around 1km and the profile structure was

385 similar to that of aerosol depolarization ratio. The subsidence of dust particles likely

386 contributed to downward transport of high-altitude O_3, thereby influencing the

387 elevated O_3 near the ground (Yang et al., 2022).
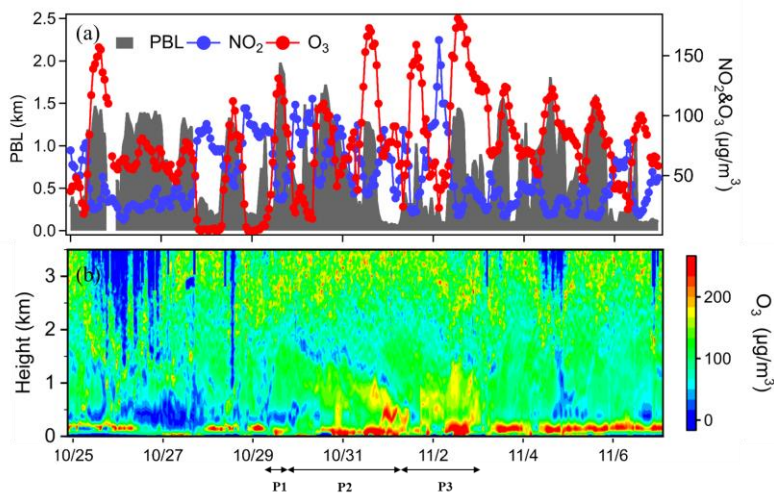
388

389 Figure 4. (a) Time-series of near surface O_3, NO_2 and planetary boundary layer height
390 (b) Vertical profiles of ozone observed by the ozone Lidar.

391

392 **3.3.2. Dust backflows during P3**

393   The dust during P3 was diagnosed as a backflow transport pathway from the

394   mainland to Shanghai through the Yellow Sea and the East China Sea, as determined

395   by the backward trajectory analysis (Figure 2f). This unconventional dust transport

396   route, termed "dust backflow", was consistent with a similar occurrence in 2014 when

397   dust from northern China detoured over Shanghai (Wang et al., 2018). In this section,

398   we have provided further evidences of the dust backflow from various aspects.

399   Figure 2f illustrates that the dust drifted away from the Shandong Peninsula, thus

400   we selected two coastal sites in Shandong province for supplementary analysis. Figure

401   S2 compares the time-series of hourly air pollutants at Qingdao, Lianyungang, and

402   Shanghai. At Qingdao and Lianyungang, high PM_{10} concentrations were observed

403   during October 30 – 31, indicating the invasion of dust in these regions. After about

404   two days, PM_{10} peaked in Shanghai on early November 2. This temporal consistency

405   aligned with the simulation duration of the backward trajectories, which lasted around

406   48 hours (Figure 2f). In Figure 9, it can be observed that in the upstream dust regions

407   (i.e., Qingdao and Lianyungang), PM_{10} varied negatively with NO_2 and CO (the

408   highlighted period in the figure). While in Shanghai, positive correlations between

409   PM_{10} and both NO_2 (R^2=0.32) and CO (R^2=0.55) indicated that the dust during P3

410   served as a carrier for gaseous pollutants rather than acting a diluter.

411

412

413
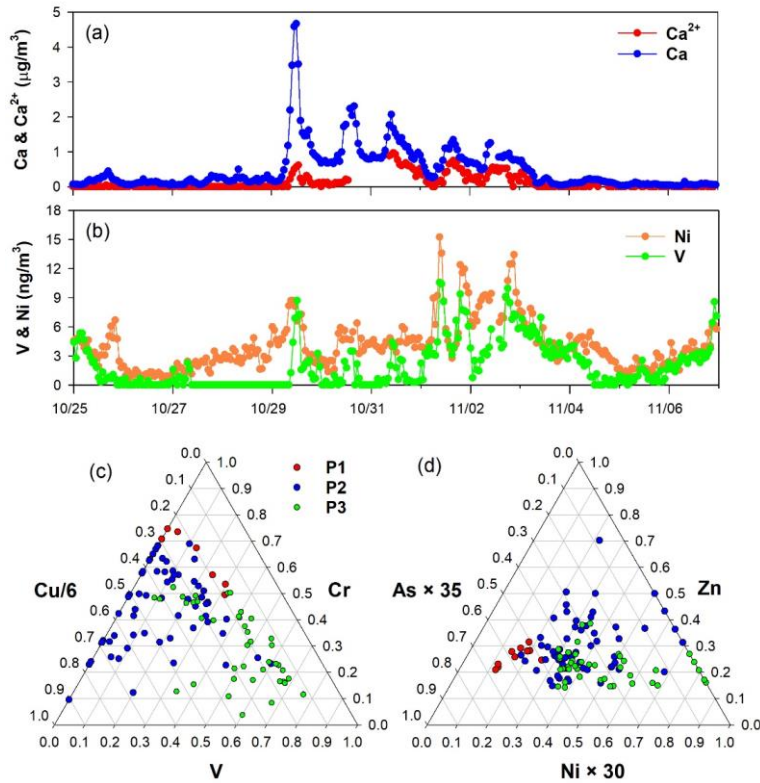
Figure 5. Time-series of (a) Ca, Ca²⁺, (b) V, and Ni during the study period. (c)

Cu-Cr-V ternary diagram and (d) As-Zn-Ni ternary diagram among the P1 – P3 dust

episodes. Due to substantial concentration differences of various elements, some

elements are artificially changed to make most scatters appear around the centroid.

Additional evidence of dust backflows was provided from the perspective of

aerosol chemical tracers. Figure 5a plots the time-series of Ca and Ca²⁺, representing

the total calcium and the soluble part of calcium, respectively. It was observed that Ca

and Ca²⁺ didn't exhibit a proportional variation trend, which should be related to the

423   solubility of calcium during different dust stages. During P1, the mean concentration of

424   Ca reached the highest of $1.63 \pm 1.53\mu g/m^3$ while Ca^{2+} was the lowest of $0.21 \pm$

425    $0.20\mu g/m^3$, thus resulting in the lowest Ca^{2+}/Ca ratio of 0.10 ± 0.08. As discussed in

426   Section 3.1, dust during P1 was the strongest and thus it contained higher fractions of

427   minerals, primarily in the form of insoluble metal oxides. The average concentrations

428   of Ca^{2+} and Ca during P2 were $0.33 \pm 0.28\mu g/m^3$ and $1.11 \pm 0.46\mu g/m^3$, respectively,

429   resulting in the higher Ca^{2+}/Ca ratio of 0.27 ± 0.20. As a comparison, the average

430   concentrations of Ca^{2+} and Ca during P3 reached $0.34 \pm 0.20\mu g/m^3$ and $0.78 \pm$

431    $0.27\mu g/m^3$, respectively, yielding the highest Ca^{2+}/Ca ratio of 0.38 ± 0.19. The

432   significantly higher solubility of calcium during P3 should be directly related to the

433   prolonged presence of dust plumes over the open ocean. The abundant water vapor over

434   the ocean could accelerate the dissolution of the insoluble components in particles

435   during the mixing between continental dust and oceanic air masses. Additionally, the

436   backflow transport pathway facilitated the entrainment of sea salts and contributed to

437   the increase of soluble calcium.

438   Figure 5b provides additional insights by displaying the time-series of V and Ni,

439   which are typical tracers of oil combustions (Becagli et al., 2012). They varied

440   significantly during the study period, and the mass concentrations of V and Ni increased

441   4 and 1.8 times during P3 compared to P2, respectively.   Consistently, the enrichment

442   factors of Ni and V displayed higher values during P3 than P1 and P2 (Figure S3). The

443   trends are substantiated in the ternary diagrams, which are commonly applied to

444   illustrate the relative abundances of three components and infer the source variations

445   (Bozlaker et al., 2019; Cwiertny et al., 2008; Laskin et al., 2005). As shown in the Cu-

446   Cr-V ternary diagram (Figure 5c), the dust samples during P1 were positioned away

447   from the V-apex. As a comparison, the dust samples during P2 exhibited greater

448   scattering, manifesting enhanced anthropogenic contributions, e.g., from chrome

449   plating industries (Hammond et al., 2008). Compared to P2, the dust samples during P3

450   moved toward the V-apex, indicating a higher contribution from oil combustions

451   (Becagli et al., 2012). A similar pattern was observed in the As-Zn-Ni ternary diagram

452   (Figure 5d). The majority of dust samples during P2 spanned across the diagram,

453   reflecting contributions from mixed anthropogenic sources. Reciprocally, P3 was closer

454   to the Ni-apex. These lines of evidences collectively confirmed that the dust had mixed

455   with pollutants from marine vessel emissions over one of the busiest international

456   shipping trade routes (Fan et al., 2016) and was subsequently transported back to

457   Shanghai.

458

459   **3.4. Formation of secondary aerosols during the dust long-range transport**

460   **3.4.1. Comparison of typical chemical tracers**

461
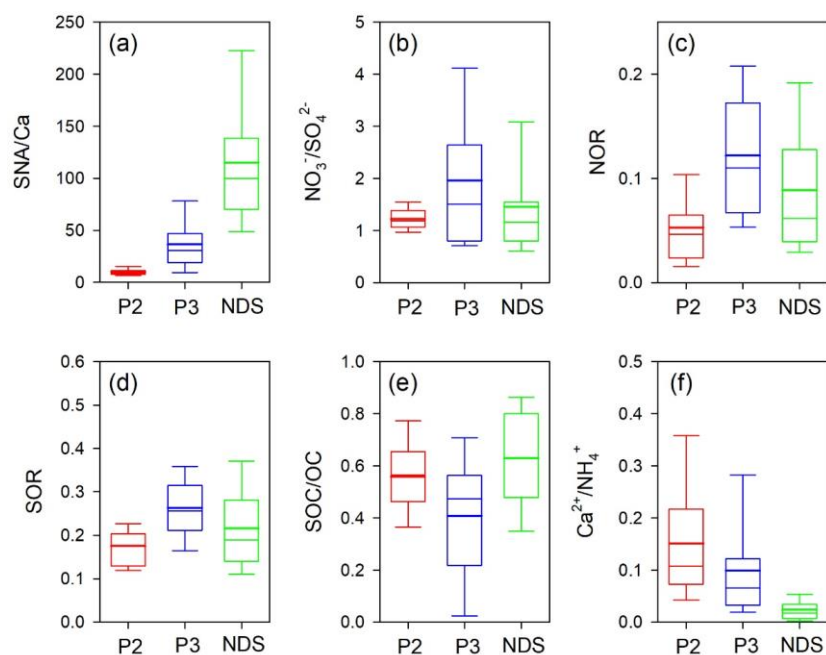
Figure 6. Box plots of (a) SNA/Ca, (b) NO_3^-/SO_4^{2-}, (c) NOR, (d) SOR, (e) SOC/OC,

and (f) Ca^{2+}/NH_4^+ during P2, P3, and NDS, respectively.

464

To delve deeper into the formation characteristics of secondary aerosols in

different stages, a variety of chemical tracers was investigated. The P1 dust stage was

excluded from statistical analysis due to its short duration and limited data availability.

Figure 6a shows the comparison of SNA/Ca ratios during P2, P3 and non-dust days

(NDS). The SNA/Ca ratio can be used to assess the relative changes between secondary

production and primary dust emission by eliminating the impact of meteorological

conditions among different periods (Zheng et al., 2015). Compared to the two dust

episodes, the SNA/Ca ratio is significantly higher during NDS. This can be attributed

to the much lower concentrations of mineral aerosols during NDS, thus resulting in the

474 higher SNA relative to Ca. In terms of comparing P2 and P3, the average SNA/Ca ratio

475 during P3 was 3 times that of P2, indicating that the formation of secondary inorganic

476 aerosols was more prominent during the dust backflow. Regarding the NO_3^-/SO_4^{2-} ratios

477 (Figure 6b), they were close between NDS and P2, with NO_3^- slightly exceeding SO_4^{2-}.

478 The range of NO_3^-/SO_4^{2-} was the largest during P3 with a mean value of around 2,

479 suggesting that the dust backflow was more conducive to the accumulation of nitrate.

480 The nitrogen oxidation ratio (NOR = $NO_3^-/(NO_3^- + NO_2)$) and the sulfur oxidation ratio

481 (SOR = $SO_4^{2-}/(SO_4^{2-} + SO_2)$) were further used to gauge the extent of nitrate and sulfate

482 formation, both showing trends of P3>NDS>P2 (Figure 6c & 6d). It should be noted

483 that NOR and SOR cannot be used to realistically characterize the extent of nitrogen

484 and sulfur oxidation during transport-dominated pollution cases, as upstream aging

485 aerosols can significantly increase the above ratios (Ji et al., 2018). In the following

486 discussion, we will focus on the formation mechanism of SNA during different dust

487 stages.

488   The results of SOC/OC ratios differed from the above analysis that SOC/OC was

489 lower during P3 than during P2 and NDS (Figure 6e), suggesting that the formation of

490 secondary organic aerosols was not favored via the dust backflow. This may be due to

491 its maritime transport pathway as the emission intensity of volatile organic compounds

492 from the ocean is much lower than that from land sources. Consequently, the lacking of

493 organic aerosol precursors could be the main cause for the lower SOC/OC ratios during

494 P3. Finally, the Ca^{2+}/NH_4^+ ratio was employed to assess the relative contributions of

495 alkaline chemical components (Figure 6f). As expected, this ratio during the two dust

496 stages was much higher than that of NDS, indicating the important contribution of dust

497 to alkaline metal ions. The Ca^{2+}/NH_4^+ ratio was higher during P3 (0.15) than during P2

498   (0.10), which aligned with the findings presented in Section 3.2.

499

500   **3.4.2. Distinct formation processes of secondary aerosols between P2 and P3**

501
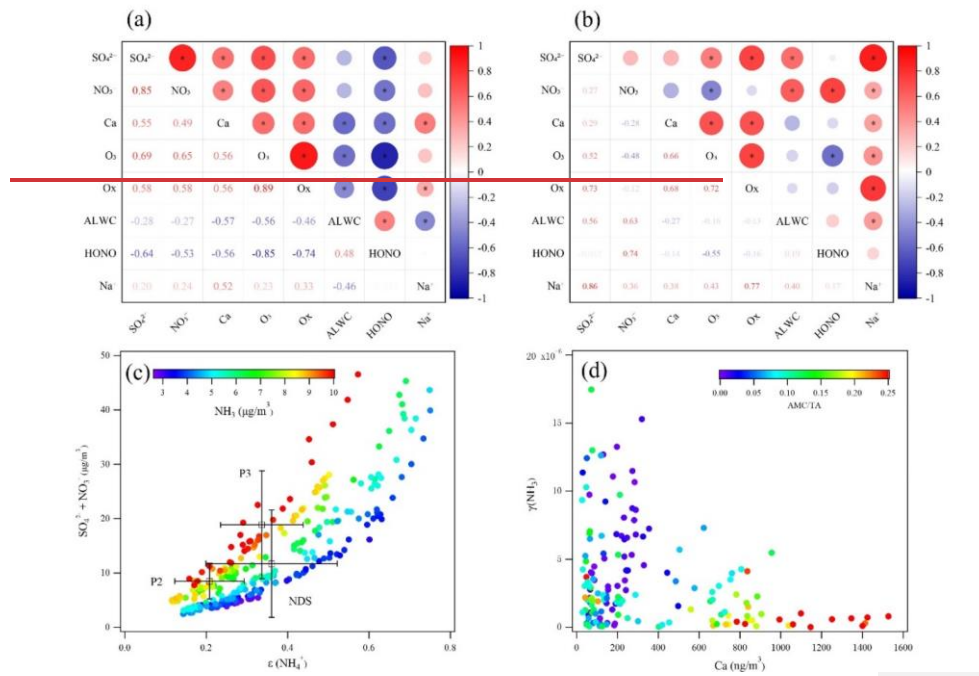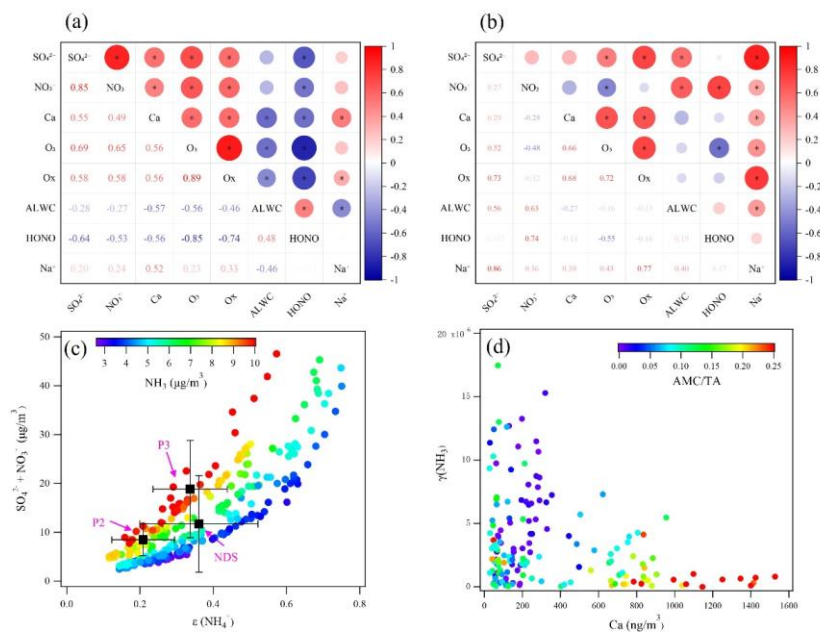
Figure 7. Correlation heatmaps during (a) P2 and (b) P3. The size of dot corresponds to the value of the correlation coefficient. The black star inside the dot means the correlation is significant ($p < 0.05$). (c) The mass concentrations of SO_4^{2-} and NO_3^- as a function of $\varepsilon(NH_4^+)$, with dots colored by the concentration of NH_3. The mean states of P2, P3, and NDS are added. Error bars denote one standard deviations. (d) The uptake coefficient of NH_3 (γ_{NH3}) on particles as a function of Ca, with dots colored by the AMC/TA molar ratios. AMC and TA denote the total molar concentrations of Na^+, K^+, Mg^{2+}, and Ca^{2+} and the total molar concentrations of anions, respectively.

In this section, we further analyze the formation mechanism and key influencing factors of secondary components during P2 and P3. Figure 7a & 7b compare the correlation heatmaps of SO_4^{2-} and NO_3^- with various parameters. During P2, both SO_4^{2-}

and NO_3^- displayed the most significant correlations with O_3 and O_x (O_3+NO_2), while even negatively correlated with ALWC. In regard of the obvious ozone enhancement phenomenon as discussed in Section 3.3.1, the photochemistry pathway for the secondary aerosol formation (e.g., S(IV) + O_3 (aq) → S(VI)) should overwhelm over the aqueous phase pathways, e.g., oxidation by H_2O_2, catalysis by tracer metals, and oxidation by NO_2photochemistry should be the main pathway for the secondary aerosol formation rather than the liquid phase processing. In addition, SO_4^{2-} and NO_3^- also showed moderate correlations with elemental Ca, suggesting that dust acted as a carrier to transport these salts, which can be derived from background minerals in dust (Wu et al., 2022) and dust heterogeneous reactions during the transport (Huang et al., 2010a).

As for P3, it showed a distinctly different correlation heatmap from P2. While SO_4^{2-} still demonstrates a correlation with O3, the relationship between NO_3^- and O_3 (as well as Ox) disappeared. On the contrary, both SO_4^{2-} and NO_3^- show significant correlations with ALWC. During P3, the average RH reached 76%, providing favorable conditions for liquid-phase reactions. Furthermore, by relating NO_3^- and the multiplication of ALWC and NO_2, the correlation coefficient ($R^2 = 0.41$) was further improved (Figure S4a). Similar results were observed by relating NO_3^- to the multiplication of ALWC and $NO_2*O_3*NO_2$ (a proxy of N_2O_5, (Huang et al., 2021)) (Figure S4b), confirming the dominant reaction pathway of nitrogen oxides to nitrate via the aqueous phase reactions. As a result, NO_3^- was also strongly correlated with HONO (Figure S4c), typically deriving from the heterogeneous reactions of NO_2 on the surface of moist particles (Alicke et al. (2002).

In addition, unlike P2, both SO_4^{2-} and NO_3^- showed moderate to significant correlations with Na^+, a tracer of sea salts (Figure 7b). Since neither SO_4^{2-} nor NO_3^-

540 correlated with Ca, it can be inferred that sea salts played a more important role in the

541 transport of air pollutant during the dust backflow over the ocean. To assess whether

542 dust or sea salts participated in the heterogeneous reactions of secondary aerosol during

543 P3, the ISORROPIA II model was run with different scenarios. Figure S5 shows the

544 model performance for SO_4^{2-}, NO_3^-, NH_4^+, and NH_3 based on the

545 $SO_4^{2-}-NO_3^--NH_4^+-Cl^--NH_3-HCl-HNO_3$ system. After adding Ca^{2+} into this

546 thermodynamic equilibrium system, the correlations between the simulations vs

547 observations for all four species were lowered with different extents (Figure S6). If Na^+

548 was added into the thermodynamic equilibrium system. the model performance was

549 slightly improved (Figure S7). This corroborated that the heterogeneous reactions on

550 dust were very limited while sea salts were intensively involved in the formation of

551 secondary inorganic aerosols during the dust backflow.

552   To further explore the influencing factors affecting the formation of secondary

553 inorganic aerosols, we examined the role of NH_3 in different stages, representing by the

554 relationship between the gas-particle partitioning of ammonia ($\varepsilon(NH_4^+)$, defined as the

555 ratio between particle phase ammonia (NH_4^+) and total ammonia ($NH_x = NH_3+NH_4^+$))

556 and the total acids ($SO_4^{2-} + NO_3^-$). As shown in Figure 7c, it is obvious that the total

557 acids strongly co-varied with $\varepsilon(NH_4^+)$. Higher $\varepsilon(NH_4^+)$ resulted in higher

558 concentrations of secondary aerosols. Moreover, under similar $\varepsilon(NH_4^+)$ conditions,

559 higher NH_3 promoted stronger formation of secondary aerosols. Thus, both NH_3 and

560 $\varepsilon(NH_4^+)$ collectively determined the aerosol formation potential. The mean states of

561 P2, P3, and NDS are compared in Figure 7c. P2 had the lowest $\varepsilon(NH_4^+)$ with the mean

562 value of 0.21, despite the relatively high concentrations of NH3 during this period (7.9

563 $\pm$ 1.0 μ g/m^3). The relatively low gas-particle partitioning of ammonia limited the

564 neutralization of the acidic components. In contrast, NH_3 during P3 was the highest

565 during the study period (9.8 ± 1.8 μg/m^3), and $\varepsilon(NH_4^+)$ (0.34) was only slightly lower

566 than that during NDS, thus effectively fostering the formation of secondary inorganic

567 aerosols.

568 To explain this phenomenon, the uptake coefficient of NH_3 (γ_{NH3}) on particles,

569 which is one of the important parameters affecting the gas-particle partitioning of

570 ammonia, was calculated. Figure 7d shows the decreasing trend of γ_{NH3} with the

571 increase of dust intensity (using Ca as an indicator). This coincided with a multi-year

572 observational study in Beijing and Shijiazhuang, where γ_{NH3} obviously increased due

573 to significant decline in alkali earth metal contents from the dust emission sources

574 during $2018 - 2020$ (Liu et al., 2022). Thus, this partially explained why $\varepsilon(NH_4^+)$ was

575 relatively low during P2, which was ascribed to the reduced uptake capacity of NH_3 on

576 particles.

577 The ion balance calculation indicated that the total anions and cations are in ideal

578 equilibrium (Figure S8, regression slope = 0.99, R^2 = 0.99), indicating that both NH_4^+

579 and alkali metal cations (including Na^+, K^+, Mg^{2+}, and Ca^{2+}) contributed to the

580 neutralization of acids to varying degrees. The ratio of alkali metal cations/total anions

581 (AMC/TA) was used to color the data points in Figure 7d, showing an opposite trend

582 between AMC/TA and γ_{NH3}. During P2, the mean value of AMC/TA reached 21%,

583 implying that the neutralization of acids by NH_3 had been significantly suppressed, thus

584 explaining `the decrease in the NH_3 uptake coefficient at high dust intensity. In contrast,

585 the AMC/TA ratio decreased to 11% during P3, indicating a reduced competition

586 between NH_3 and the alkali dust components. Finally, we also compared the aerosol pH

587 at different stages, which was 3.2, 3.0, and 2.8 during P2, P3, and NDS, respectively.

588 The relatively high aerosol acidity at P3 and NDS favored the uptake of alkaline gases

589 (Liu et al., 2022), which also contributed to the higher (γ_{NH3}) at these two stages.

590

591 **3.5. Estimation of transported and secondarily formed particles during P3**

592 As discussed in previous sections, the aerosols observed during P3 could originate

593 from both aged aerosols transported via the dust backflows and secondary formation.

594 In this section, we aimed to estimate the contribution of transport and secondary

595 formation to the main aerosol species, respectively, based on the simultaneous

596 measurements at the Pudong site and the Lianyungang site. As discussed in Section

597 3.4.1, Lianyungang acted as an upstream region where dust drifted away from the

598 mainland. The duration of dust observed at Lianyungang was approximately from 5:00

599 on October 30 to 16:00 on October 31, about 46 hours ahead of the dust invasion

600 observed at Pudong (Figure S2).

601 To assess the extents of transported air pollutants, black carbon (BC) was used as

602 a reference aerosol component. As shown in Figure S9, one BC pollution episode on

603 October 30 at Lianyungang was observed. Correspondingly, another BC pollution

604 episode emerged at Pudong on November 2after about 46 hours. Since the air mass

605 trajectory from Lianyungang to Pudong predominantly traversed over the ocean, and

606 considering that BC has no secondary sources, it can be reasonably assumed that the

607 differences of BC concentrations between these two sites were ascribed to the removal

608 processes of particles.

609 To determine the removal fractions of aerosols during dust transport, we first

610 defined the average concentrations of various aerosol components during the preceding

611 five hours of the dust at Pudong as their background concentrations. Then, a coefficient

612   k was derived to calculate the removal fractions of aerosols during the dust transport as

613   below.

614

615 $$k = \frac{AV_{LYG,BC} - (AV_{PD,BC} - BKG_{PD,BC})}{AV_{LYG,BC}}$$

616   (3)

617     $AV_{LYG,BC}$ and $AV_{PD,BC}$ represent the average concentration of BC at Lianyungang

618   and Pudong during their respective dust period. $BKG_{PD,BC}$ represents the background

619   concentration of BC at Pudong. Assuming that other aerosol species were removed with

620   a similar efficiency as BC, the amounts of transported aerosol species from

621   Lianyungang to Pudong can be estimated as below.

622     $TP_{PD,i} = AV_{LYG,i} \times (1 - k)$ (4)

623     $TP_{PD,i}$ represents the transported amounts of aerosol species i. 1-k represents the

624   transport fraction of aerosols. Then, the secondarily formed aerosol species i at Pudong

625   can be calculated as below.

626     $SF_{PD,i} = AV_{PD,i} - BKG_{PD,i} - TP_{PD,i}$ (5)

627   Figure 8 shows the results of the transported and the secondarily formed aerosol

628   species during P3. It was calculated that the secondarily formed and transported NO_3^-

629   averaged 6.8μg/m^3 and 4.7μg/m^3, accounting for about 45% and 31% of its total mass

630   concentration, respectively. This was consistent with the earlier analysis that a

631   considerable portion of nitrate was formed through the aqueous phase secondary

632   formation. In contrast, it was calculated that the transported SO_4^{2-} accounted for about

633   42% of its total mass concentration, while the secondarily formed SO_4^{2-} was almost

634   negligible. This was also consistent with the phenomenon that SO_4^{2-} correlated

635   significantly with Na^+ (Figure 6b). As for NH_4^+, it exhibited a similar apportionment as

636   NO_3^-, with the secondarily formed and transported NH_4^+ accounting for about 35% and

Formatted: Font: Italic

Formatted: Font: Not Italic, Not Superscript/Subscript

637 28% of its total mass concentration, respectively. Compared to NO_3^- and NH_4^+, OM was

638 more dominated by transport (57%) while its secondary formation only accounted for

639 about 13%. It should be noted that the simple method devised in this study may have

640 inherent uncertainties. Considering the prolonged duration of the dust event, it is

641 possible that certain dust particles lingered over the open ocean. Consequently, the

642 contributions attributed to aerosol transport should be considered as a conservative

643 estimate or lower bound, rather than an exhaustive assessment.

644

645

646
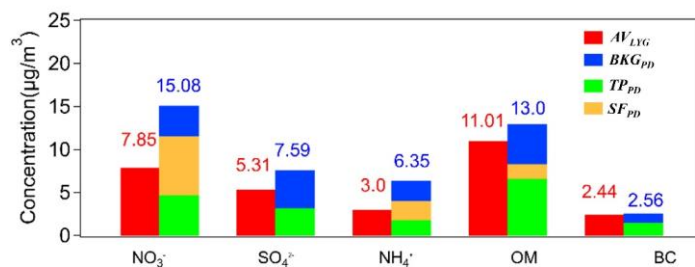
647

648 Figure 8. The apportioned concentrations of the major aerosol species during P3.

649

650 **4. Conclusion**

651 During October 29 to November 2, 2019, a long-lasting dust event was observed in

652 Shanghai based on a synergy measurement of near surface air pollutants, aerosol lidar,

653 wind profiling lidar, and air masses trajectory modeling. During the whole dust period,

654 the mean concentrations of $PM_{2.5}$ and PM_{10} reached 53.3 ± 20.5μg/m³ and 172.4 ±

655 70.2μg/m³. Different from most dust events, this dust event was characterized of

656 exceptionally high relative humidity, (71 ± 26%) and low wind speed, and relatively

657 high concentrations of gaseous pollutants. (0.54 ± 0.59m/s). Due to this stagnant

658 synoptic condition, the mean concentrations of main gaseous pollutants such as O_3, SO_2,

659 and NO_2 reached 86.0 ± 47.8μg/m³, 11.8 ± 3.4μg/m³, and 63.3 ± 27.9μg/m³,

660 respectively, even higher than those during the non-dust period.

661 The dust event was divided into three stages from P1 – P3. P1 was a short dust episode

662 when wind profiles showed dominant northwest winds from the ground to the altitudes

663 of around 2km, indicating the presence of adue to the strong cold frontsynoptic system.

664 P2 was a dust episode when RH was moderately high of 70 ± 26% and the

665 southeasterlies prevailed with partial air masses from coastal regions. P3 was a rarely

666 observed dust backflow transport episode. The air masses originated from the Shandong

667 Peninsula and the northern region of Jiangsu province, and then migrated over the

668 Yellow Sea and the East China Sea. RH reached the highest of 76 ± 24% among the

669 three stages of the dust event.

670 During P2, mineral aerosols accounted for 33% in $PM_{2.5}$, the highest among all

671 three stages. aAbnormally high O_3 concentrations were observed, much higher than the

672 non-dust days. This was partiallywhich could be due to the weak synoptic system as

673 well as that exerted weak dilution effect on the local air pollutants. The ozone lidar

674 observed that the subsidence of dust particles probably down drafted high-altitude O_3

675 along with the subsidence of dust particlesand also contributed to the high O_3 near the

676 ground. As a result, Ssulfate and nitrate moderately correlated with O_3 while had

677 almost no correlation with ALWC, indicating that the formation of secondary aerosols

678 during P2 should be mainly promoted via the gas-phase oxidations. –

679 During P3, a special phenomenon of dust backflow was observed and confirmed

680 by various evidences. Two upstream sites (Qingdao and Lianyungang) showed dust

681 ~~occurrences about 48 hours ahead that of Shanghai, consistent with the transport~~

682 ~~duration of the dust backflow from the Shandong Peninsula to Shanghai over the Yellow~~

683 ~~Sea and the East China Sea. As a result, t~~The highest Ca^{2+}/Ca ratio was observed due

684 to that the lingerer of dust plumes over the open ocean. Moreover, contributions of V

685 and Ni significantly increased, indicating the mixing between dust and marine vessel

686 emissions. Different from P2, nitrate significantly correlated with ALWC but not with

687 O_3~~,~~, indicating its aqueous-phase reaction pathway. Also, sulfate and nitrate exhibited

688 moderate to strong correlations with Na^+, suggesting sea salts as a medium for the

689 heterogeneous reactions.

690 By analyzing various chemical tracers, the formation extent of SNA was found

691 much stronger during P3 than during P2. Both NH_3 and $\varepsilon(NH_4^+)$

692 $(NH_4^+/(NH_3+NH_4^+))$ determined the concentrations of SNA. To explain the relatively

693 high $\varepsilon(NH_4^+)$ values during P3, the uptake coefficient of NH_3 (γ_{NH3}) on particles is

694 calculated. γ_{NH3} negatively varied with the intensity of dust, which were attributed to

695 two factors. Higher contributions of alkali metal components suppressed the

696 neutralization capacity of NH_3 on acids, thereby lowering γ_{NH3} during P2. Also,

697 relatively high aerosol pH during P2 didn't facilitate the uptake of NH_3 and the

698 subsequent aerosol formation.

699 Based on a simplified method, the amounts of transported and secondarily formed

700 particles during P3 were quantified. It was calculated that about 45% and 31% of NO_3^-

701 was contributed by secondary formation and transport, respectively. In contrast, the

702 transported SO_4^{2-} accounted for about 42% of its total mass concentration while the rest

703 was from its background concentration with negligible secondary formation. OM was

704 dominated by transport (57%) while its secondary formation only accounted for about

705   13%.

706

707   **Data Availability Statement**

708   All data used in this study can be requested upon the corresponding author

709   (huangkan@fudan.edu.cn).

710

711   **Author contributions**

712   KH, QF, and YD designed this study. JH, FY, YL, and JC performed data

713   collection. DL and KH performed data analysis and wrote the paper. All have

714   commented on and reviewed the paper.

715

716   **Competing interests**

717   The authors declare that they have no conflict of interest.

718

719   **Acknowledgments**

720   This work was financially supported by the National Key R&D Plan programs

721   (2023YFE0102500) and National Science Foundation of China (42175119).

722
723

724   **References**
725   Alicke, B., Platt, U., and Stutz, J.: Impact of nitrous acid photolysis on the total hydroxyl
726   radical budget during the Limitation of Oxidant Production/Pianura Padana Produzione di
727   Ozono study in Milan, J. Geophys. Res.-Atmos., 107, 18, 10.1029/2000jd000075, 2002.
728   Ansari, A. S. and Pandis, S. N.: An analysis of four models predicting the partitioning of
729   semivolatile inorganic aerosol components, Aerosol Science And Technology, 31, 129-153,
730   10.1080/027868299304200, 1999.
731   Arimoto, R., Ray, B. J., Lewis, N. F., Tomza, U., and Duce, R. A.: Mass-particle size
732   distributions of atmospheric dust and the dry deposition of dust to the remote ocean, J. Geophys.

733 Res.-Atmos., 102, 15867-15874, 10.1029/97jd00796, 1997.

734   Barkley, A., Olson, N., Prospero, J., Gatineau, A., Panechou, K., Maynard, N.,
735 Blackwelder, P., China, S., Ault, A., and Gaston, C.: Atmospheric Transport of North African
736 Dust‑Bearing Supermicron Freshwater Diatoms to South America: Implications for Iron
737 Transport to the Equatorial North Atlantic Ocean, Geophysical Research Letters, 48,
738 10.1029/2020GL090476, 2021.

739   Becagli, S., Sferlazzo, D. M., Pace, G., di Sarra, A., Bommarito, C., Calzolai, G., Ghedini,
740 C., Lucarelli, F., Meloni, D., Monteleone, F., Severi, M., Traversi, R., and Udisti, R.: Evidence
741 for heavy fuel oil combustion aerosols from chemical analyses at the island of Lampedusa: a
742 possible large role of ships emissions in the Mediterranean, Atmos. Chem. Phys., 12, 3479-
743 3492, 10.5194/acp-12-3479-2012, 2012.

744   Benas, N., Mourtzanou, E., Kouvarakis, G., Bais, A., Mihalopoulos, N., and Vardavas, I.:
745 Surface ozone photolysis rate trends in the Eastern Mediterranean: Modeling the effects of
746 aerosols and total column ozone based on Terra MODIS data, Atmospheric Environment, 74,
747 1-9, 10.1016/j.atmosenv.2013.03.019, 2013.

748   Bernard, F., Cazaunau, M., Grosselin, B., Zhou, B., Zheng, J., Liang, P., Zhang, Y., Ye, X.,
749 Daële, V., Mu, Y., Zhang, R., Chen, J., and Mellouki, A.: Measurements of nitrous acid (HONO)
750 in urban area of Shanghai, China, Environmental Science and Pollution Research, 23, 5818-
751 5829, 10.1007/s11356-015-5797-4, 2016.

752   Bozlaker, A., Prospero, J. M., Price, J., and Chellam, S.: Identifying and Quantifying the
753 Impacts of Advected North African Dust on the Concentration and Composition of Airborne
754 Fine Particulate Matter in Houston and Galveston, Texas, J Geophys Res-Atmos, 124, 12282-
755 12300, 10.1029/2019jd030792, 2019.

756   Cwiertny, D. M., Baltrusaitis, J., Hunter, G. J., Laskin, A., Scherer, M. M., and Grassian,
757 V. H.: Characterization and acid-mobilization study of iron-containing mineral dust source
758 materials, J Geophys Res-Atmos, 113, Artn D05202

759   10.1029/2007jd009332, 2008.

760   Dall'Osto, M., Harrison, R. M., Coe, H., and Williams, P.: Real-time secondary aerosol
761 formation during a fog event in London, Atmospheric Chemistry And Physics, 9, 2459-2469,
762 10.5194/acp-9-2459-2009, 2009.

763   Draxler, R. R., and G. D. Hess, 1998: An overview of the HYSPLIT_4 modeling
764 system for trajectories, dispersion, and deposition. Aust. Meteor. Mag., 47, 295–308.

765   Fan, H., Zhao, C., Yang, Y., and Yang, X.: Spatio-Temporal Variations of the
766 PM2.5/PM10 Ratios and Its Application to Air Pollution Type Classification in China, Frontiers
767 in Environmental Science, 2021, https://doi.org/10.3389/fenvs.2021.692440.

768

769   Fan, Q. Z., Zhang, Y., Ma, W. C., Ma, H. X., Feng, J. L., Yu, Q., Yang, X., Ng, S. K. W.,
770   Fu, Q. Y., and Chen, L. M.: Spatial and Seasonal Dynamics of Ship Emissions over the Yangtze
771   River Delta and East China Sea and Their Potential Environmental Influence, Environmental
772   Science & Technology, 50, 1322-1329, 10.1021/acs.est.5b03965, 2016.

773   Feng, X., Mao, R., Gong, D.-Y., Zhao, C., Wu, C., Zhao, C., Wu, G., Lin, Z., Liu, X., Wang,
774   K., and Sun, Y.: Increased Dust Aerosols in the High Troposphere Over the Tibetan Plateau
775   From 1990s to 2000s, Journal of Geophysical Research: Atmospheres, 125, e2020JD032807,
776   https://doi.org/10.1029/2020JD032807, 2020.

777   Ge, X. L., He, Y. A., Sun, Y. L., Xu, J. Z., Wang, J. F., Shen, Y. F., and Chen, M. D.:
778   Characteristics and Formation Mechanisms of Fine Particulate Nitrate in Typical Urban Areas
779   in China, Atmosphere, 8, 12, 10.3390/atmos8030062, 2017.

780   Ginoux, P., Prospero, J. M., Torres, O., and Chin, M.: Long-term simulation of global dust
781   distribution with the GOCART model: correlation with North Atlantic Oscillation,
782   Environmental Modelling & Software, 19, 113-128, https://doi.org/10.1016/S1364-
783   8152(03)00114-2, 2004.

784   Goodman, M. M., Carling, G. T., Fernandez, D. P., Rey, K. A., Hale, C. A., Bickmore, B.
785   R., Nelson, S. T., and Munroe, J. S.: Trace element chemistry of atmospheric deposition along
786   the Wasatch Front (Utah, USA) reflects regional playa dust and local urban aerosols, Chemical
787   Geology, 530, 10.1016/j.chemgeo.2019.119317, 2019.

788   Hammond, D. M., Dvonch, J. T., Keeler, G. J., Parker, E. A., Kamal, A. S., Barres, J. A.,
789   Yip, F. Y., and Brakefield-Caldwell, W.: Sources of ambient fine particulate matter at two
790   community   sites   in   Detroit,   Michigan,   Atmos.   Environ.,   42,   720-732,
791   10.1016/j.atmosenv.2007.09.065, 2008.

792   Hertel, O., Skjoth, C. A., Reis, S., Bleeker, A., Harrison, R. M., Cape, J. N., Fowler, D.,
793   Skiba, U., Simpson, D., Jickells, T., Kulmala, M., Gyldenkaerne, S., Sorensen, L. L., Erisman,
794   J. W., and Sutton, M. A.: Governing processes for reactive nitrogen compounds in the European
795   atmosphere, Biogeosciences, 9, 4921-4954, 10.5194/bg-9-4921-2012, 2012.

796   Hilario, M. R. A., Cruz, M. T., Cambaliza, M. O. L., Reid, J. S., Xian, P., Simpas, J. B.,
797   Lagrosas, N. D., Uy, S. N. Y., Cliff, S., and Zhao, Y. J.: Investigating size-segregated sources
798   of elemental composition of particulate matter in the South China Sea during the 2011 Vasco
799   cruise, Atmospheric Chemistry And Physics, 20, 1255-1276, 10.5194/acp-20-1255-2020, 2020.

800   Hsu, S.-C., Lee, C. S. L., Huh, C.-A., Shaheen, R., Lin, F.-J., Liu, S. C., Liang, M.-C., and
801   Tao, J.: Ammonium deficiency caused by heterogeneous reactions during a super Asian dust
802   episode,   Journal   of   Geophysical   Research: Atmospheres,   119,   6803-6817,
803   10.1002/2013jd021096, 2014.

804   Huang, K., Fu, J. S., Lin, N.-H., Wang, S.-H., Dong, X., and Wang, G.: Superposition of

Gobi Dust and Southeast Asian Biomass Burning: The Effect of Multisource Long-Range Transport on Aerosol Optical Properties and Regional Meteorology Modification, Journal of Geophysical Research: Atmospheres, 124, 9464-9483, https://doi.org/10.1029/2018JD030241, 2019.

Huang, K., Zhuang, G., Li, J., Wang, Q., Sun, Y., Lin, Y., and Fu, J. S.: Mixing of Asian dust with pollution aerosol and the transformation of aerosol components during the dust storm over China in spring 2007, Journal of Geophysical Research, 115, 10.1029/2009jd013145, 2010a.

~~Huang, K., Zhuang, G. S., Li, J. A., Wang, Q. Z., Sun, Y. L., Lin, Y. F., and Fu, J. S.: Mixing of Asian dust with pollution aerosol and the transformation of aerosol components during the dust storm over China in spring 2007, J Geophys Res Atmos, 115, Artn D00k13~~
~~10.1029/2009jd013145, 2010b.~~

Huang, X., Ding, A. J., Gao, J., Zheng, B., Zhou, D. R., Qi, X. M., Tang, R., Wang, J. P., Ren, C. H., Nie, W., Chi, X. G., Xu, Z., Chen, L. D., Li, Y. Y., Che, F., Pang, N. N., Wang, H. K., Tong, D., Qin, W., Cheng, W., Liu, W. J., Fu, Q. Y., Liu, B. X., Chai, F. H., Davis, S. J., Zhang, Q., and He, K. B.: Enhanced secondary pollution offset reduction of primary emissions during COVID-19 lockdown in China, Natl Sci Rev, 8, ARTN nwaa137
10.1093/nsr/nwaa137, 2021.

Jeong, G. Y.: Bulk and single-particle mineralogy of Asian dust and a comparison with its source soils, J Geophys Res-Atmos, 113, Artn D02208
10.1029/2007jd008606, 2008.

Ji, Y., Qin, X. F., Wang, B., Xu, J., Shen, J. D., Chen, J. M., Huang, K., Deng, C. R., Yan, R. C., Xu, K. E., and Zhang, T.: Counteractive effects of regional transport and emission control on the formation of fine particles: a case study during the Hangzhou G20 summit, Atmos Chem Phys, 18, 13581-13600, 10.5194/acp-18-13581-2018, 2018.

Jiang, Y., Zhuang, G., Wang, Q., Huang, K., Deng, C., Yu, G., Xu, C., Fu, Q., Lin, Y., Fu, J. S., Li, M., and Zhou, Z.: Impact of mixed anthropogenic and natural emissions on air quality and eco-environment—the major water-soluble components in aerosols from northwest to offshore isle, Air Quality, Atmosphere & Health, 11, 521-534, 10.1007/s11869-018-0557-5, 2018.

Laskin, A., Wietsma, T. W., Krueger, B. J., and Grassian, V. H.: Heterogeneous chemistry of individual mineral dust particles with nitric acid: A combined CCSEM/EDX, ESEM, and ICP-MS study, J Geophys Res-Atmos, 110, Artn D10208
10.1029/2004jd005206, 2005.

Li, T., Wang, Y., Zhou, J., Wang, T., Ding, A. J., Nie, W., Xue, L. K., Wang, X. F., and Wang, W. X.: Evolution of trace elements in the planetary boundary layer in southern China:

Effects of dust storms and aerosol-cloud interactions, J Geophys Res-Atmos, 122, 3492-3506, 10.1002/2016jd025541, 2017.

Liang, Y., Liu, Y., Wang, H., Li, L., Duan, Y., and Lu, K.: Regional characteristics of ground-level ozone in Shanghai based on PCA analysis, Acta Scientiae Circumstantiae, 38, 3807-3815, 2018.

Liu, H., Liu, S., Xue, B., Lv, Z., Meng, Z., Yang, X., Xue, T., Yu, Q., and He, K.: Ground-level ozone pollution and its health impacts in China, Atmospheric Environment, 173, 223-230, https://doi.org/10.1016/j.atmosenv.2017.11.014, 2018.

Liu, J., Ding, J., Rexiding, M., Li, X., Zhang, J., Ran, S., Bao, Q., and Ge, X.: Characteristics of dust aerosols and identification of dust sources in Xinjiang, China, Atmospheric Environment, 262, 118651, https://doi.org/10.1016/j.atmosenv.2021.118651, 2021.

Liu, Y. C., Zhan, J. L., Zheng, F. X., Song, B. Y., Zhang, Y. S., Ma, W., Hua, C. J., Xie, J. L., Bao, X. L., Yan, C., Bianchi, F., Petaja, T., Ding, A. J., Song, Y., He, H., and Kulmala, M.: Dust emission reduction enhanced gas-to-particle conversion of ammonia in the North China Plain, Nat Commun, 13, ARTN 6887
10.1038/s41467-022-34733-4, 2022.

Ma, S. Q., Zhang, X. L., Gao, C., Tong, Q. S., Xiu, A. J., Zhao, H. M., and Zhang, S. C.: Simulating Performance of CHIMERE on a Late Autumnal Dust Storm over Northern China, Sustainability-Basel, 11, ARTN 1074
10.3390/su11041074, 2019.

Malm, W. C., Sisler, J. F., Huffman, D., Eldred, R. A., and Cahill, T. A.: Spatial and seasonal trends in particle concentration and optical extinction in the United States, Journal of Geophysical Research: Atmospheres, 99, 1347-1370, https://doi.org/10.1029/93JD02916, 1994.

Mcneil, W. R. and Carswell, A. I.: Lidar Polarization Studies of Troposphere, Appl. Opt., 14, 2158–2168, 1975.

Mentel, T. F., Bleilebens, D., and Wahner, A.: A study of nighttime nitrogen oxide oxidation in a large reaction chamber—the fate of NO2, N2O5, HNO3, and O3 at different humidities, Atmospheric Environment, 30, 4007-4020, https://doi.org/10.1016/1352-2310(96)00117-3, 1996.

Nagashima, K., Suzuki, Y., Irino, T., Nakagawa, T., Tada, R., Hara, Y., Yamada, K., and Kurosaki, Y.: Asian dust transport during the last century recorded in Lake Suigetsu sediments, Geophysical Research Letters, 43, 2835-2842, https://doi.org/10.1002/2015GL067589, 2016.

Nenes, A., Pandis, S. N., and Pilinis, C.: ISORROPIA: A new thermodynamic equilibrium model for multiphase multicomponent inorganic aerosols, Aquat. Geochem., 4, 123-152, 10.1023/a:1009604003981, 1998.

Patel, A. and Rastogi, N.: Chemical Composition and Oxidative Potential of Atmospheric PM10 over the Arabian Sea, ACS Earth Space Chem., 4, 112-121, 10.1021/acsearthspacechem.9b00285, 2020.

Perez, N., Pey, J., Reche, C., Cortes, J., Alastuey, A., and Querol, X.: Impact of harbour emissions on ambient PM10 and PM2.5 in Barcelona (Spain): Evidences of secondary aerosol formation within the urban area, Science Of the Total Environment, 571, 237-250, 10.1016/j.scitotenv.2016.07.025, 2016.

Petetin, H., Sciare, J., Bressi, M., Gros, V., Rosso, A., Sanchez, O., Sarda-Estève, R., Petit, J. E., and Beekmann, M.: Assessing the ammonium nitrate formation regime in the Paris megacity and its representation in the CHIMERE model, Atmos. Chem. Phys., 16, 10419-10440, 10.5194/acp-16-10419-2016, 2016.

Shen, L., Zhao, C., Ma, Z., Li, Z., Li, J., and Wang, K.: Observed decrease of summer sea-land breeze in Shanghai from 1994 to 2014 and its association with urbanization, Atmospheric Research, 227, 198-209, https://doi.org/10.1016/j.atmosres.2019.05.007, 2019.

Shimizu, A., N. Sugimoto, I. Matsui, K. Arao, I. Uno, T. Murayama, N. Kagawa, K. Aoki, A. Uchiyama, and A. Yamazaki (2004), Continuous observations of Asian dust and other aerosols by polarization lidars in China and Japan during ACE-Asia, J. Geophys. Res.,109, D19S17, doi:10.1029/ 2002JD003253.

Song, S., Gao, M., Xu, W., Shao, J., Shi, G., Wang, S., Wang, Y., Sun, Y., and McElroy, M. B.: Fine-particle pH for Beijing winter haze as inferred from different thermodynamic equilibrium models, Atmos. Chem. Phys., 18, 7423-7438, 10.5194/acp-18-7423-2018, 2018.

Stein, A. F., Draxler, R. R., Rolph, G. D., Stunder, B. J. B., Cohen, M. D., Ngan, F., NOAA's HYSPLIT Atmospheric Transport and Dispersion Modeling System, Bulletin of the American Meteorological Society, 2015, 2059–2077.

Su, L., Yuan, Z., Fung, J. C. H., and Lau, A. K. H.: A comparison of HYSPLIT backward trajectories generated from two GDAS datasets, Science of The Total Environment, 506-507, 527-537, https://doi.org/10.1016/j.scitotenv.2014.11.072, 2015.

Sun, P., Nie, W., Wang, T., Chi, X., Huang, X., Xu, Z., Zhu, C., Wang, L., Qi, X., Zhang, Q., and Ding, A.: Impact of air transport and secondary formation on haze pollution in the Yangtze River Delta: In situ online observations in Shanghai and Nanjing, Atmospheric Environment, 225, 117350, https://doi.org/10.1016/j.atmosenv.2020.117350, 2020.

Tang, M., Cziczo, D. J., and Grassian, V. H.: Interactions of Water with Mineral Dust Aerosol: Water Adsorption, Hygroscopicity, Cloud Condensation, and Ice Nucleation, Chemical Reviews, 116, 4205-4259, 10.1021/acs.chemrev.5b00529, 2016.

Tang, M. J., Huang, X., Lu, K. D., Ge, M. F., Li, Y. J., Cheng, P., Zhu, T., Ding, A. J., Zhang, Y. H., Gligorovski, S., Song, W., Ding, X., Bi, X. H., and Wang, X. M.: Heterogeneous

reactions of mineral dust aerosol: implications for tropospheric oxidation capacity, Atmos Chem Phys, 17, 11727-11777, 10.5194/acp-17-11727-2017, 2017.

Tian, R., Ma, X., Sha, T., Pan, X., and Wang, Z.: Exploring dust heterogeneous chemistry over China: Insights from field observation and GEOS-Chem simulation, Science of The Total Environment, 798, 149307, https://doi.org/10.1016/j.scitotenv.2021.149307, 2021.

Vicars, W. C. and Sickman, J. O.: Mineral dust transport to the Sierra Nevada, California: Loading rates and potential source areas, Journal of Geophysical Research, 116, 10.1029/2010jg001394, 2011.

Wang, G., Chen, J., Xu, J., Yun, L., Zhang, M., Li, H., Qin, X., Deng, C., Zheng, H., Gui, H., Liu, J., and Huang, K.: Atmospheric processing at the sea-land interface over the South China Sea: secondary aerosol formation, aerosol acidity, and role of sea salts, Journal of Geophysical Research: Atmospheres, n/a, e2021JD036255, https://doi.org/10.1029/2021JD036255,

Wang, G. C., Chen, J., Xu, J., Yun, L., Zhang, M. D., Li, H., Qin, X. F., Deng, C. R., Zheng, H. T., Gui, H. Q., Liu, J. G., and Huang, K.: Atmospheric Processing at the Sea-Land Interface Over the South China Sea: Secondary Aerosol Formation, Aerosol Acidity, and Role of Sea Salts, J. Geophys. Res.-Atmos., 127, 10.1029/2021jd036255, 2022a.

Wang, G. H., Cheng, C. L., Huang, Y., Tao, J., Ren, Y. Q., Wu, F., Meng, J. J., Li, J. J., Cheng, Y. T., Cao, J. J., Liu, S. X., Zhang, T., Zhang, R., and Chen, Y. B.: Evolution of aerosol chemistry in Xi'an, inland China, during the dust storm period of 2013-Part 1: Sources, chemical forms and formation mechanisms of nitrate and sulfate, Atmospheric Chemistry And Physics, 14, 11571-11585, 10.5194/acp-14-11571-2014, 2014.

Wang, H. C. and Lu, K. D.: Determination and Parameterization of the Heterogeneous Uptake Coefficient of Dinitrogen Pentoxide (N2O5), Prog Chem, 28, 917-933, 10.7536/Pc151225, 2016.

Wang, J. J., Zhang, M. G., Bai, X. L., Tan, H. J., Li, S., Liu, J. P., Zhang, R., Wolters, M. A., Qin, X. Y., Zhang, M. M., Lin, H. M., Li, Y. N., Li, J., and Chen, L. Q.: Large-scale transport of PM2.5 in the lower troposphere during winter cold surges in China, Sci Rep, 7, 10, 10.1038/s41598-017-13217-2, 2017.

Wang, L., Du, H., Chen, J., Zhang, M., Huang, X., Tan, H., Kong, L., and Geng, F.: Consecutive transport of anthropogenic air masses and dust storm plume: Two case events at Shanghai, China, Atmospheric Research, 127, 22-33, https://doi.org/10.1016/j.atmosres.2013.02.011, 2013.

Wang, N., Zheng, P., Wang, R., Wei, B., An, Z., Li, M., Xie, J., Wang, Z., Wang, H., and He, M.: Homogeneous and heterogeneous atmospheric ozonolysis of acrylonitrile on the mineral dust aerosols surface, Journal of Environmental Chemical Engineering, 9, 106654,

https://doi.org/10.1016/j.jece.2021.106654, 2021.

Wang, Q., Wang, X., Huang, R., Wu, J., Xiao, Y., Hu, M., Fu, Q., Duan, Y., and Chen, J.-M.: Regional Transport of PM 2.5 and O 3 Based on Complex Network Method and Chemical Transport Model in the Yangtze River Delta, China, Journal of Geophysical Research: Atmospheres, 127, 10.1029/2021JD034807, 2022b.

Wang, Z., Pan, X. L., Uno, I., Chen, X. S., Yamamoto, S., Zheng, H. T., Li, J., and Wang, Z. F.: Importance of mineral dust and anthropogenic pollutants mixing during a long-lasting high PM event over East Asia, Environ. Pollut., 234, 368-378, 10.1016/j.envpol.2017.11.068, 2018.

Wang, Z. L., Huang, X., Wang, N., Xu, J. W., and Ding, A. J.: Aerosol-Radiation Interactions of Dust Storm Deteriorate Particle and Ozone Pollution in East China, J Geophys Res-Atmos, 125, ARTN e2020JD033601

10.1029/2020JD033601, 2020.

West, J. J., Ansari, A. S., and Pandis, S. N.: Marginal PM25: Nonlinear Aerosol Mass Response to Sulfate Reductions in the Eastern United States, Journal of the Air & Waste Management Association, 49, 1415-1424, 10.1080/10473289.1999.10463973, 1999.

Wu, C., Zhang, S., Wang, G., Lv, S., Li, D., Liu, L., Li, J., Liu, S., Du, W., Meng, J., Qiao, L., Zhou, M., Huang, C., and Wang, H.: Efficient Heterogeneous Formation of Ammonium Nitrate on the Saline Mineral Particle Surface in the Atmosphere of East Asia during Dust Storm Periods, Environmental Science & Technology, 54, 15622-15630, 10.1021/acs.est.0c04544, 2020.

Wu, F., Cheng, Y., Hu, T. F., Song, N., Zhang, F., Shi, Z. B., Ho, S. S. H., Cao, J. J., and Zhang, D. Z.: Saltation-Sandblasting Processes Driving Enrichment of Water- Soluble Salts in Mineral Dust, Environ Sci Tech Let, 9, 921-928, 10.1021/acs.estlett.2c00652, 2022.

Xie, S. D., Yu, T., Zhang, Y. H., Zeng, L. M., Qi, L., and Tang, X. Y.: Characteristics of PM10, SO2, NO, and O-3 in ambient air during the dust storm period in Beijing, Sci Total Environ, 345, 153-164, 10.1016/j.scitotenv.2004.10.013, 2005.

Xu, J., Chen, J., Zhao, N., Wang, G. C., Yu, G. Y., Li, H., Huo, J. T., Lin, Y. F., Fu, Q. Y., Guo, H. Y., Deng, C. R., Lee, S. H., Chen, J. M., and Huang, K.: Importance of gas-particle partitioning of ammonia in haze formation in the rural agricultural environment, Atmospheric Chemistry and Physics, 20, 7259-7269, 10.5194/acp-20-7259-2020, 2020.

Xu, P., Zhang, J. K., Ji, D. S., Liu, Z. R., Tang, G. Q., Hu, B., Jiang, C. S., and Wang, Y. S.: Evaluating the Effects of Springtime Dust Storms over Beijing and the Associated Characteristics of Sub-Micron Aerosol, Aerosol Air Qual Res, 17, 680-692, 10.4209/aaqr.2016.05.0195, 2017.

Yang, Y., Wang, Z. L., Lou, S. J., Xue, L., Lu, J. P., Wang, H. Y., Wang, J. D., Ding, A. J.,

985 and Huang, X.: Strong ozone intrusions associated with super dust storms in East Asia, Atmos
986 Environ, 290, ARTN 119355
987   10.1016/j.atmosenv.2022.119355, 2022.
988   Yu, S. C., Dennis, R., Roselle, S., Nenes, A., Walker, J., Eder, B., Schere, K., Swall, J., and
989 Robarge, W.: An assessment of the ability of three-dimensional air quality models with current
990 thermodynamic equilibrium models to predict aerosol NO3, J. Geophys. Res.-Atmos., 110,
991 10.1029/2004jd004718, 2005.
992   Zhang, D., Iwasaka, Y., Shi, G., Zang, J., Hu, M., and Li, C.: Separated status of the natural
993 dust plume and polluted air masses in an Asian dust storm event at coastal areas of China,
994 Journal of Geophysical Research (Atmospheres), 110, D06302, 10.1029/2004jd005305, 2005.
995   Zhang, S. P., Xing, J., Sarwar, G., Ge, Y. L., He, H., Duan, F. K., Zhao, Y., He, K. B., Zhu,
996 L. D., and Chu, B. W.: Parameterization of heterogeneous reaction of SO2 to sulfate on dust
997 with coexistence of NH3 and NO2 under different humidity conditions, Atmos Environ, 208,
998 133-140, 10.1016/j.atmosenv.2019.04.004, 2019.
999   Zhang, X. L., Wu, G. J., Zhang, C. L., Xu, T. L., and Zhou, Q. Q.: What is the real role of
1000 iron oxides in the optical properties of dust aerosols?, Atmos Chem Phys, 15, 12159-12177,
1001 10.5194/acp-15-12159-2015, 2015.
1002   Zhao, D., Xin, J., Wang, W., Jia, D., Wang, Z., Xiao, H., Liu, C., Zhou, J., Tong, L., Ma,
1003 Y., Wen, T.-X., Wu, F.-K., and Wang, L.: Effects of the sea-land breeze on coastal ozone
1004 pollution in the Yangtze River Delta, Science of The Total Environment, 807,
1005 10.1016/j.scitotenv.2021.150306, 2021.
1006   Zheng, G. J., Duan, F. K., Su, H., Ma, Y. L., Cheng, Y., Zheng, B., Zhang, Q., Huang, T.,
1007 Kimoto, T., Chang, D., Poschl, U., Cheng, Y. F., and He, K. B.: Exploring the severe winter
1008 haze in Beijing: the impact of synoptic weather, regional transport and heterogeneous reactions,
1009 Atmos Chem Phys, 15, 2969-2983, 10.5194/acp-15-2969-2015, 2015.
1010   Zheng, Y., Zhao, T., Che, H., Liu, Y., Han, Y., Liu, C., Xiong, J., Liu, J., and Zhou, Y.: A
1011 20-year simulated climatology of global dust aerosol deposition, Science of The Total
1012 Environment, 557-558, 861-868, https://doi.org/10.1016/j.scitotenv.2016.03.086, 2016.
1013